

# SCIENTIFIC REPORTS

OPEN

## Effects of strain relaxation in $\text{Pr}_{0.67}\text{Sr}_{0.33}\text{MnO}_3$ films probed by polarization dependent X-ray absorption near edge structure

Received: 28 May 2015  
Accepted: 21 December 2015  
Published: 28 January 2016

Bangmin Zhang<sup>1</sup>, Jingsheng Chen<sup>1</sup>, Ping Yang<sup>2</sup>, Xiao Chi<sup>2,3</sup>, Weinan Lin<sup>1</sup>, T. Venkatesan<sup>1,3,4,5</sup>, Cheng-Jun Sun<sup>6</sup>, Steve M. Heald<sup>6</sup> & Gan Moog Chow<sup>1</sup>

The Mn *K* edge X-ray absorption near edge structure (XANES) of  $\text{Pr}_{0.67}\text{Sr}_{0.33}\text{MnO}_3$  films with different thicknesses on (001)  $\text{LaAlO}_3$  substrate was measured, and the effects of strain relaxation on film properties were investigated. The films showed in-plane compressive and out-of-plane tensile strains. Strain relaxation occurred with increasing film thickness, affecting both lattice constant and  $\text{MnO}_6$  octahedral rotation. In polarization dependent XANES measurements using in-plane (parallel) and out-of-plane (perpendicular) geometries, the different values of absorption resonance energy  $E_r$  confirmed the film anisotropy. The values of  $E_r$  along these two directions shifted towards each other with increasing film thickness. Correlating with X-ray diffraction (XRD) results it is suggested that the strain relaxation decreased the local anisotropy and corresponding probability of electronic charge transfer between Mn *3d* and O *2p* orbitals along the in-plane and out-of-plane directions. The XANES results were used to explain the film-thickness dependent magnetic and transport properties.

The perovskite manganites ( $\text{Re}_{1-x}\text{A}_x\text{MnO}_3$ ), where *Re* is a trivalent rare earth, and *A* is a divalent metal exhibit a range of interesting properties<sup>1–2</sup> such as high spin polarization and colossal magnetoresistance (CMR). Manganites are potential candidates for resistance random access memories (RRAM) in the next generation of non-volatile memories<sup>3–5</sup>. The electronic structure plays an important role<sup>4</sup> in resistance switching of RRAM<sup>6–8</sup>. The electronic structure of manganite is correlated with the local environment<sup>9</sup> that affects material properties<sup>10</sup>. For example, the intersite hopping of Mn *3d* electrons through the bridging oxygen *2p* orbital affects the double-exchange coupling strength<sup>11</sup> and Curie temperature  $T_c$ . Crystal structure and electronic structure are correlated through strong electron-phonon coupling in manganites<sup>1</sup>. Thin films grown on single crystal substrates are normally strained due to lattice-mismatch between the film and substrate. The crystal structure and octahedral rotation of thin films may therefore differ from that of bulk<sup>12</sup>. Strain relaxation occurs gradually and continuously with increasing film thickness, leading to film-thickness dependent  $T_c$ <sup>1,9,12</sup>. Polarization dependent X-ray absorption structure (XAS) may be used to probe the film-thickness dependent electronic structure. Correlating the electronic structure with the crystal structure, material properties such as magnetoresistance may be better understood.

X-ray absorption near edge structure (XANES) provides insight into the electronic structure of the absorbing atom<sup>13</sup>. For manganites, the absorbing ion of interest is Mn in the  $\text{MnO}_6$  octahedron. The Mn XAS may be collected either by total electron yield (TEY) mode or total fluorescence yield (TFY) mode<sup>14</sup>. Due to the low fluorescence signal intensity in the soft X-ray region<sup>15</sup>, the TFY mode cannot be used. Instead the total electron yield (TEY) mode may be employed to collect the Mn *L* edge (~640 eV) XAS, however, the signal sampling depth is limited to only a few nanometers near the surface<sup>10,14</sup>. The surface-sensitive information from TEY may not

<sup>1</sup>Department of Materials Science & Engineering, National University of Singapore, 117576, Singapore. <sup>2</sup>Singapore Synchrotron Light Source (SSLs), National University of Singapore, 5 Research Link, 117603 Singapore. <sup>3</sup>Department of Physics, National University of Singapore, 117542, Singapore. <sup>4</sup>NUSNNI-Nanocore, National University of Singapore, 117411, Singapore. <sup>5</sup>Department of Electrical & Computer Engineering, National University of Singapore, 117576, Singapore. <sup>6</sup>Advanced Photon Source, Argonne National Laboratory, Argonne, IL 60439, USA. Correspondence and requests for materials should be addressed to C.-J.S. (email: cjsun@aps.anl.gov) or G.M.C. (email: msecgm@nus.edu.sg)

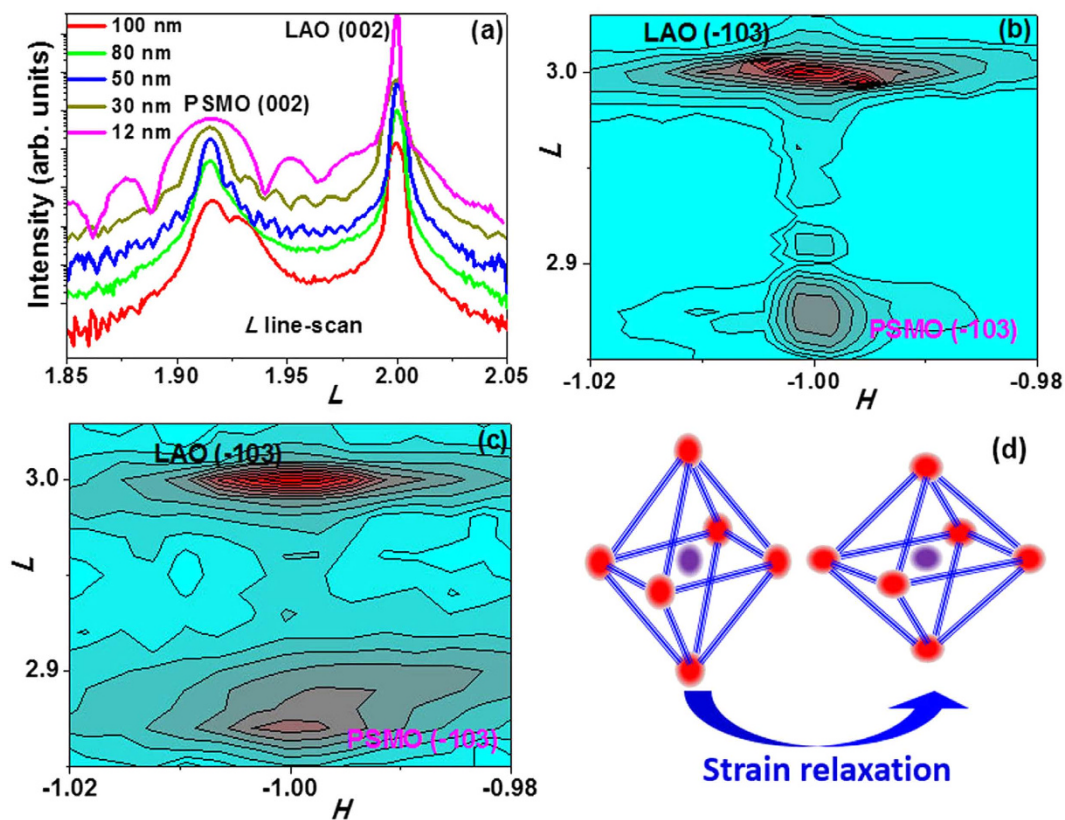


**Figure 1.** (a) (00l) scan of PSMO films with different thicknesses on LAO substrate; reciprocal spacing mapping around  $(-103)$  for (b) 12-nm and (c) 100-nm film; (d) illustration of strain relaxation in tetragonal ratio of  $\text{MnO}_6$  octahedron.

necessarily be representative for thick films. Additional information and discussion of Mn  $L$  edge data are found in Supplementary Figure S1 online.

In the hard X-ray region, the quality of the TFY signal is enhanced, and therefore may be used to collect the Mn  $K$  edge ( $\sim 6.5$  keV) signal<sup>16</sup>. The TFY signal is bulk sensitive<sup>17</sup> and is suitable for investigating the effects of strain relaxation in films of the various thicknesses (12 to 100-nm) as used in our current study. The main absorption structure in the Mn  $K$  edge XANES is due to the excitation of a Mn core  $1s$  electron to empty  $4p$  orbitals<sup>18</sup>, which is sensitive to the local environment around the absorbing atom. For example, due to hybridization between Mn  $3d$  orbitals and O  $2p$  orbitals, there exists a mixture of O  $2p$  orbitals with Mn  $3d$  orbitals. The electronic structure with  $n$  electrons in Mn  $3d$  orbitals may be described as a mixture of two configurations<sup>19–22</sup>:  $3d^n L$  and  $3d^{n+1} \underline{L}$ .  $L$  refers to the O ligand surrounding the Mn ion, and  $\underline{L}$  indicates O ligand with one electron hole resulting from the electron transfer from O  $2p$  to empty Mn  $3d$  orbitals. After X-ray absorption, two electronic configurations exist for the final states:  $3d^n L 4p^1$  and  $3d^{n+1} \underline{L} 4p^1$ . These final states may be revealed in the fine structure of XANES. The effects of strain relaxation on film properties may be investigated using the sensitivity of XANES to the crystal structure.

In this work we report the Mn  $K$  edge X-ray absorption near edge structure (XANES) of  $\text{Pr}_{0.67}\text{Sr}_{0.33}\text{MnO}_3$  (PSMO) films of different thicknesses on (001)  $\text{LaAlO}_3$  (LAO) substrates. The narrow bandwidth manganite has high strain sensitivity<sup>23</sup>. Bulk PSMO has a smaller bandwidth than that of the  $\text{La}_{1-x}\text{Sr}_x\text{MnO}_3$  system<sup>1</sup>. Thus, bulk PSMO may find potential application due to its high transition temperature, i.e. its ferromagnetic metal (FM)-to-paramagnetic insulator (PI) phase transition at  $\sim 300$  K<sup>24,25</sup>. Our results show that the PSMO films deposited on LAO substrate experienced in-plane compressive strain and out-of-plane tensile strain. In polarization dependent measurements, the in-plane (parallel) and out-of-plane (perpendicular) XANES showed anisotropic properties with different absorption energies  $E_r$  (peak point). With increasing film thickness, the difference of  $E_r$  between these two polarization dependent measurements decreased. Correlating with the XRD results, it is suggested that the strain relaxation weakened the local anisotropy and the corresponding probability of charge transfer between Mn  $3d$  and O  $2p$  along in-plane and out-of-plane directions. This is responsible for the change of  $E_r$  with increasing film thickness. The transport and magnetic properties also changed with strain relaxation, mediated by the change of electronic structure.

## Results

The XRD results of PSMO films are shown in Fig. 1(a–c). For the 12-nm film, the in-plane lattice constant ( $3.790$  Å) was the same as that of the LAO substrate (as shown in Fig. 1(b)), indicating that the PSMO film was fully strained by the LAO substrate. The calculated<sup>26</sup> out-of-plane lattice constant ( $3.958$  Å) from the (002) peak

Thickness (nm)	a (Å)	c (Å)	c/a	MnO <sub>6</sub> Tilt	T <sub>c</sub> /T <sub>c,30nm</sub>	
					Exp.	Cal.
12	3.790	3.957	1.044	a <sup>0</sup> a <sup>0</sup> c <sup>-</sup>	—	—
30	3.790	3.959	1.045	a <sup>0</sup> a <sup>0</sup> c <sup>-</sup>	1	1
50	3.790	3.958	1.044	a <sup>-</sup> a <sup>-</sup> c <sup>-</sup>	1.013	1.006
80	3.792 (L)	3.956 (L)	1.043 (L)	a <sup>-</sup> a <sup>-</sup> c <sup>-</sup>	1.221	1.040
	3.796 (R)	3.947(R)	1.040 (R)			
100	3.792 (L)	3.954(L)	1.043 (L)	a <sup>-</sup> a <sup>-</sup> c <sup>-</sup>	1.275	1.102
	3.807 (R)	3.924(R)	1.031 (R)			

**Table 1. Summary of averaged lattice constant, tetragonal ratio, measured (Exp.) and calculated (Cal.) Curie temperature T<sub>c</sub> of PSMO films with different thicknesses.** T<sub>c</sub> was normalized to that of the 30-nm film. For the lattice constants of the 80-nm and 100-nm films, the in-plane lattice constant was calculated based on volume-conservation. Refer to the text for more details.

was larger than the bulk value (3.860 Å). The in-plane compressive strain (−1.8%) between the PSMO film and LAO substrate elongated the out-of-plane lattice<sup>27</sup>. In the 80-nm and the 100-nm films, the (00*l*) curves (Fig. 1a) indicate more than one peak. The results were fitted into two components (*P1* and *P2*) as shown in Supplementary Figure S2 online. The reciprocal space mapping around the (−103) peak and *L* scan indicate that the in-plane and out-of-plane lattice constants are not uniform for the 100-nm film, as a result of strain relaxation in this thicker film (Fig. 1b,c). However, due to the volume-averaged XRD signal and the overlapping peaks, the differentiation of the value of *H* for these two parts are difficult. To resolve this challenge, volume conservation was assumed. The in-plane lattice constants of *P1* and *P2* components were calculated based on the volume-conservation assumption<sup>28</sup>, as shown in Table 1. Previous work revealed that moving from the LAO substrate into the PSMO film, the *c* value of the PSMO film changed gradually from 3.790 Å of substrate to that of PSMO (>3.950 Å) in ~15 unit cells<sup>27</sup>. This could cause a peak shift and broadening. As indicated in Table 1, the lower *c* value in the 12-nm film compared to that in 30 nm film could be attributed to this non-uniform region. The effects of this region on film properties will be discussed later. With the increase of film thickness from 30 nm, the strain relaxed partially and the out-of-plane lattice parameter *c* decreased gradually. Due to strain relaxation, the tetragonal ratio *c/a* (Table 1) of the PSMO film changed, and the corresponding change of the MnO<sub>6</sub> octahedron is illustrated in Fig. 1(d). Previous work of epitaxial films on different substrates<sup>29–32</sup> showed that the tetragonal *c/a* ratio had a direct influence on electronic structure and anisotropy in the electronic hopping integral.

The strain affects not only the lattice constant, but also the MnO<sub>6</sub> rotation in the PSMO films. In Fig. 2(a–c), half-integer diffraction was measured to determine the octahedral rotation. According to Glazer's notation<sup>33–36</sup>, the MnO<sub>6</sub> rotation pattern in the 12-nm film is a<sup>0</sup>a<sup>0</sup>c<sup>-</sup>. With increasing film thickness, one additional peak (0.5 0.5 1.5) gradually appeared and became obvious in the 50-nm film, as shown in Fig. 2(c). Note that the intensity of this peak (indicated by the purple arrow in Fig. 2(c) for films ≥ 50 nm) is weak. This suggests that the MnO<sub>6</sub> rotation in the thick films (≥ 50 nm) became a<sup>-</sup>a<sup>-</sup>c<sup>-</sup>. The effects of strain relaxation on the MnO<sub>6</sub> rotation is illustrated in Fig. 2(d). The measured rotation of AlO<sub>6</sub> in the LAO substrate was a<sup>-</sup>a<sup>-</sup>a<sup>-</sup> in our study, consistent with the reported results<sup>21</sup>. The in-plane compressive strain suppressed the octahedron tilt around the two in-plane (*x* and *y*) axes. The rotation around the two in-plane axes gradually occurred with partial relaxation of in-plane compressive strain in the thick films. This phenomenon is consistent with previous work<sup>21</sup> that demonstrated the existence of in-plane rotation (a<sup>-</sup>/b<sup>-</sup>) in strain-free and in-plane tensile strain cases. Based on the integer and half-integer diffraction results, the crystal structure of PSMO films with different thicknesses changed drastically, affecting the corresponding electronic structure and other film properties.

The properties of manganites are strongly coupled with the electronic structure. XANES is able to detect the local environment of the absorbing atom and electronic structure. Polarization dependent XANES was used to study the effects of strain on the electronic structure. The polarization dependent XANES is defined as follows: in parallel measurement (||), the polarization vector (*E* vector) of the X-rays was in the film plane; in perpendicular case (⊥), the polarization vector was perpendicular to the film plane. The polarization-dependent Mn *K* edge XANES of the 12-nm PSMO film is shown in Fig. 3. In this study, we only focused on the main absorption edge at ~ 6555 eV, which is due to the electronic excitation from the Mn core 1s orbital to empty 4*p* orbitals<sup>18</sup>. The absorption intensity revealed the unoccupied states of the Mn 4*p* orbitals.

As shown in Fig. 3, the resonance energy *E<sub>r</sub>* (peak point) was different between the two polarization dependent measurements (|| and ⊥). The PSMO film experienced in-plane compressive and out-of-plane tensile strains as shown from the XRD measurements. In the parallel measurement, the polarization direction was along the in-plane compressive strain direction giving a higher *E<sub>r</sub>* value (6555.8 eV). In the perpendicular measurement, the polarization direction was along the out-of-plane tensile strain direction with a lower *E<sub>r</sub>* (6554.9 eV). The derivative curves of Mn *K* edge XANES are shown in Fig. 3(b). In the parallel measurement, the Mn *K* edge XANES revealed two sub-peaks at 6552.4 eV (B1) and 6553.7 eV (B2), respectively. In the perpendicular case, the intensity of the lower energy peak (B1) increased, whereas the higher energy peak (B2) disappeared. There are several possible reasons for the origin of these two sub-peaks. (1) The coexistence of the Mn<sup>3+</sup> and Mn<sup>4+</sup> ions in the film<sup>37,38</sup>. The ratio of B1/B2 should be similar in both parallel and perpendicular measurements if the ions with different chemical valences are the main factor, whereas our experimental results show different B1/B2 ratios for films with different thicknesses. (2) The energy splitting of Mn empty 4*p<sub>x</sub>*, 4*p<sub>y</sub>*, 4*p<sub>z</sub>* levels due to the anisotropy of the local environment<sup>39</sup>. The strain relaxation in thick film changed its crystal structure, and the position of B1

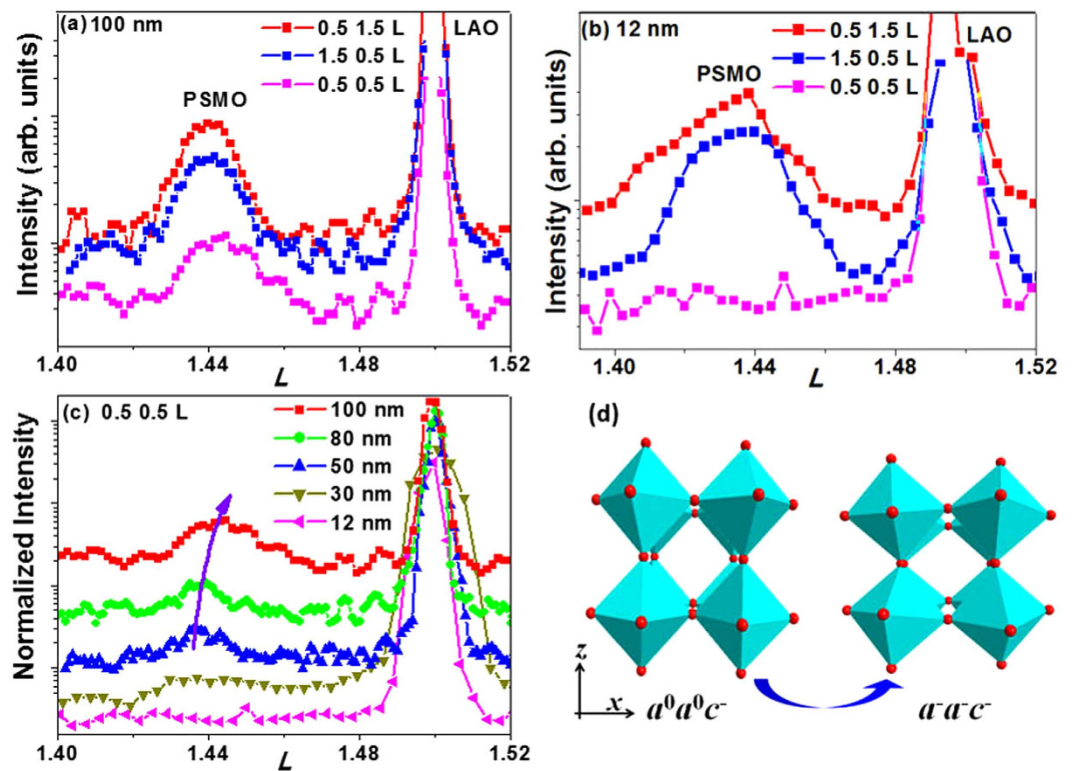


Figure 2. Half-integer diffraction peak of (a) 100-nm and (b) 12-nm PSMO films; (c) the (0.5 0.5  $l$ ) peak of PSMO film with different thicknesses. The curve was normalized to the LAO (002) peak; (d) illustration of the effect of strain relaxation on  $\text{MnO}_6$  octahedral rotation pattern.

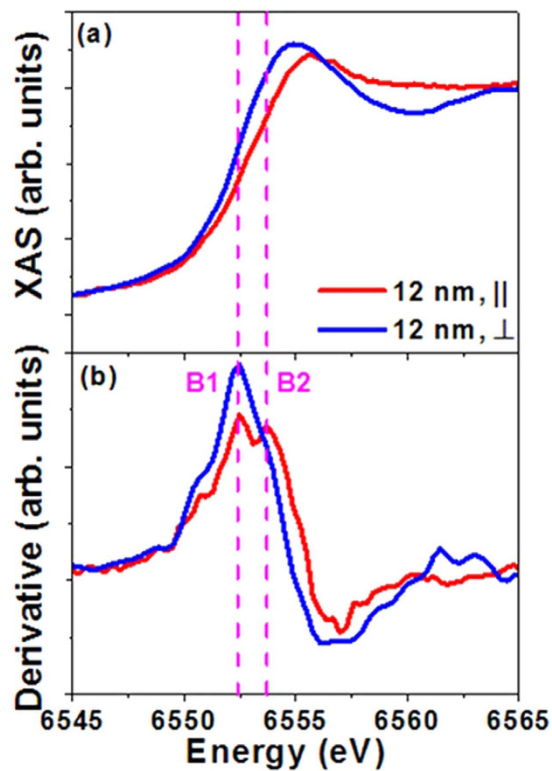
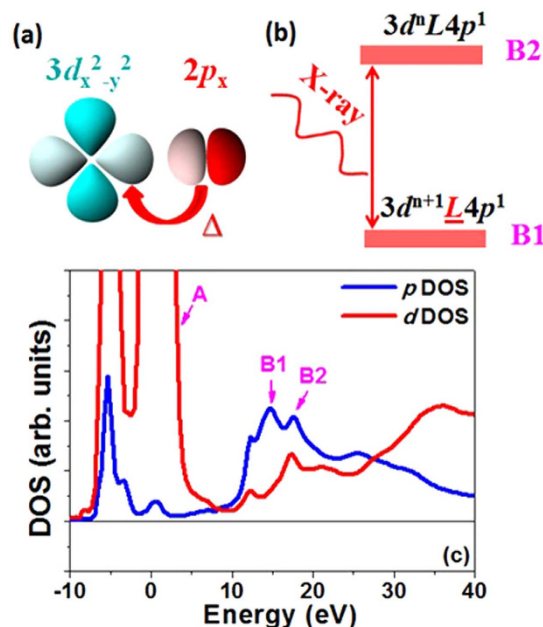


Figure 3. (a) Polarized Mn K edge XANES and (b) corresponding derivative curves for the 12-nm PSMO film.



**Figure 4.** Illustration of (a) charge transfer ( $\Delta$ ) between Mn  $3d$  and O  $2p$  orbitals, and (b) final electronic configuration after X-ray absorption. Refer to the text for details; (c) the calculated  $p$  and  $d$ -projected density of states (DOS) of the Mn atom for the 12-nm PSMO film.

and B2 should change accordingly if the strain-induced splitting of Mn  $4p$  energy level was responsible. However, the positions of B1 and B2 peaks from the derivative curves did not change with different thicknesses. (3) The electronic charge transfer between the Mn  $3d$  and O  $2p$  orbitals<sup>40</sup> (Fig. 4(a)). The anisotropic strain along in-plane and out-of-plane directions induces large anisotropy in the local environment in the two directions. The hybridization between Mn  $3d$  orbitals and O  $2p$  orbitals then becomes anisotropic due to the difference of orbital overlap along these two different directions<sup>41</sup>. During the X-ray absorption process (from Mn core  $1s$  to Mn  $4p$ ), the charge transfer (from O  $2p$  to Mn  $3d$ ) existed simultaneously. The final state may be viewed as a mixture of two electronic configurations<sup>19–21</sup>:  $3d^nL4p^1$ , and  $3d^{n+1}\underline{L}4p^1$ . The  $L$  refers to the O ligands, and  $\underline{L}$  indicates one hole in the O ligands, resulting from the electron transfer from O  $2p$  to empty Mn  $3d$  orbitals. In the  $3d^{n+1}\underline{L}4p^1$  configuration, the Coulomb interaction between the Mn  $1s$  core hole and the extra  $3d$  electron lowers the total energy from electron transfer<sup>15</sup>. Hence, the lower energy B1 peak corresponded to the photon absorption leading to the final configuration  $3d^{n+1}\underline{L}4p^1$  as shown in Fig. 4(b), and the higher energy B2 peak corresponds to the photon absorption leading to the final configuration  $3d^nL4p^1$ . This assignment was further supported by the density of states (DOS) calculated using the FEFF8.4 code. The 118 atomic cluster was built based on XRD results and the simulation details were expressed elsewhere<sup>42,43</sup>. Fig. 4(c) shows the  $p$ ,  $d$ -projected density of states (DOS) on the Mn site for a 12-nm PSMO film with the Fermi level set to zero. The peak A in Mn  $3d$  orbitals is assigned to the pre-edge of Mn  $K$  edge XANES, while the peak B1 and B2 in  $p$  orbitals is assigned to the main  $K$  edge absorption<sup>19</sup>. The splitting of the DOS around B1 and B2 causes the multiple peaks in the X-ray absorption curve.

Taking the perpendicular measurement as an example, the excited Mn  $1s$  core electron will fill the empty  $4p_z$  orbital. In this situation, the dominant charge transfer is the in-plane process (Fig. 4(a)), filling the Mn  $3d_{x^2-y^2}$  orbital through O  $2p_x, 2p_y$  orbitals. Although the Mn  $3d$  orbitals hybridized with 6 oxygen atoms in all  $x, y, z$  directions, the possibility of electron transfer from oxygen  $2p$  to fill the Mn  $3d_{3z^2-r^2}$  is limited due to the strong Coulomb interaction between the excited  $1s$  core electron at  $4p_z$  and the electron at the  $3d_{3z^2-r^2}$  orbital (in the event that the transferred electron occupied the  $3d_{3z^2-r^2}$  orbital). In this case, the in-plane compressive strain enhances the hybridization between Mn  $3d$  and O  $2p$  orbitals, resulting in strong absorption corresponding to the  $3d^{n+1}\underline{L}4p^1$  (B1 peak) configuration. Similarly, in the parallel measurement, the dominant charge transfer was the out-of-plane process, filling the Mn  $3d_{x^2-y^2}$  orbital through O  $2p_z$  orbitals. The out-of-plane tensile strain weakens the hybridization between Mn and O, limiting the absorption corresponding to the  $3d^{n+1}\underline{L}4p^1$  (B1 peak) configuration.

The two B1 and B2 sub-peaks in the derivative curve (Fig. 3d) indicate that the shape of the Mn  $K$  edge XANES has two contributions, and the relative ratio of the B1/ B2 peak intensity affects the maximum position of XANES ( $E_r$ ). Both the crystal structure and the charge transfer were affected by the strain relaxation, which is revealed by  $E_r$ . The Mn  $K$  edge XANES of PSMO films of different thicknesses is shown in Fig. 5(a). The difference of  $E_r$  of two polarization dependent measurements, summarized in Fig. 5(b), showed a decrease with increasing film thickness. This phenomenon may be understood as follows: with the existence of strain relaxation, the anisotropy of the local environment along the in-plane and out-of-plane directions decreased as demonstrated in Fig. 1(d). Thus there is a decrease in the difference of probability of electronic charge transfer along the two directions (parallel direction from O  $2p_{x,y}$  to Mn  $3d_{x^2-y^2}$ ; and perpendicular direction from O  $2p_z$  to Mn  $3d_{3z^2-r^2}$ ).

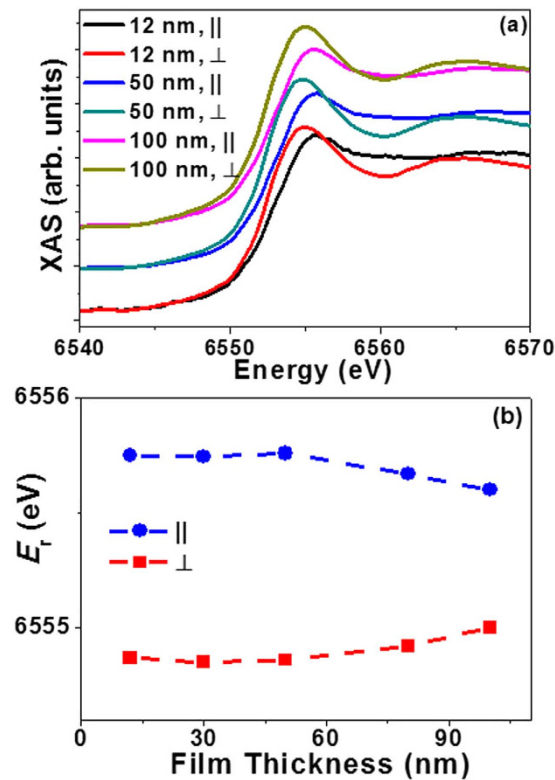


**Figure 5.** (a) Polarized Mn K edge XANES for PSMO films with different thicknesses; (b) summary of  $E_r$  from the parallel and perpendicular measurements with varying film thickness. The dashed lines are viewing guides.

The difference of relative ratio of B1/B2 peak in XANES is thus decreased, and the resonance energy  $E_r$  along the two directions shifts towards each other with increasing film thickness.

## Discussion

The polarization dependent XANES is sensitive to the electronic structure due to the hybridization between Mn 3d and O 2p orbitals. In the 12-nm film, the in-plane charge transfer predominated over that in the out-of-plane direction. With increasing film thickness, both the in-plane and out-of-plane charge transfer became important. Figure 6(a–c) shows the magnetoresistance ( $MR = (\rho_H - \rho_0)/\rho_0$ ) curves for the PSMO films. Large MR values existed near  $T_c$  in all films. At low temperature the MR value increased with decreasing film thickness. It has been identified that with decreasing film thickness the quantum interference effects (QIE) from electron-electron interactions and weak localization<sup>44,45</sup> become more important at low temperature. The dimensionality of the system, i.e. 3-dimensional (3D) and 2-dimensional (2D), influences the temperature dependent resistance. In the 2D system, the QIE has a logarithmic dependence ( $\ln T$ ) as follows<sup>44,45</sup>:

$$\rho(T) = \frac{1}{\sigma_0 + B \ln T} + AT^n \quad (1)$$

In the 3D system, the QIE changes as  $T^{p/2}$ . The fitting parameter  $p = 1$  has been used to determine the change from 3D to 2D<sup>43</sup>, as shown below:

$$\rho(T) = \frac{1}{\sigma_0 + CT^{1/2}} + AT^n \quad (2)$$

where  $\sigma_0$ ,  $A$ ,  $B$ ,  $C$ , and  $n$  are free fitting parameters. In our work, the low temperature ( $< 60$  K) transport data were fitted according to the two above equations. The normalized  $\chi^2 = \left(\frac{1}{N}\right) \sum_{i=1}^N \left[ \frac{(\rho_{raw}^i - \rho_{fit}^i)^2}{(\rho_{fit}^i)^2} \right]$  characterizes how well the experimental data is fitted; a smaller value indicates a better fit. In this equation,  $N$  is the number of data points,  $\rho_{raw}$  and  $\rho_{fit}$  are measured and fitted resistivities, respectively. The fitting details are found in Supplementary Figure S3 online. It was observed that the  $\ln T$  fitting was better with a smaller  $\chi^2$  for the 12-nm film; for thicker films (80 nm), the  $T^{1/2}$  showed a better fit. For the 100-nm film, the absolute difference between the two  $\chi^2$  values was very small, probably indicating the decreasing role played by the QIE correction terms in equations (1) and (2)<sup>44</sup>. In other words, the two equations using the QIE correction terms may no longer be applicable in thick films. The fitting data suggest that in the 12-nm film, the 2D QIE seemed to emerge. Figure 6(c)

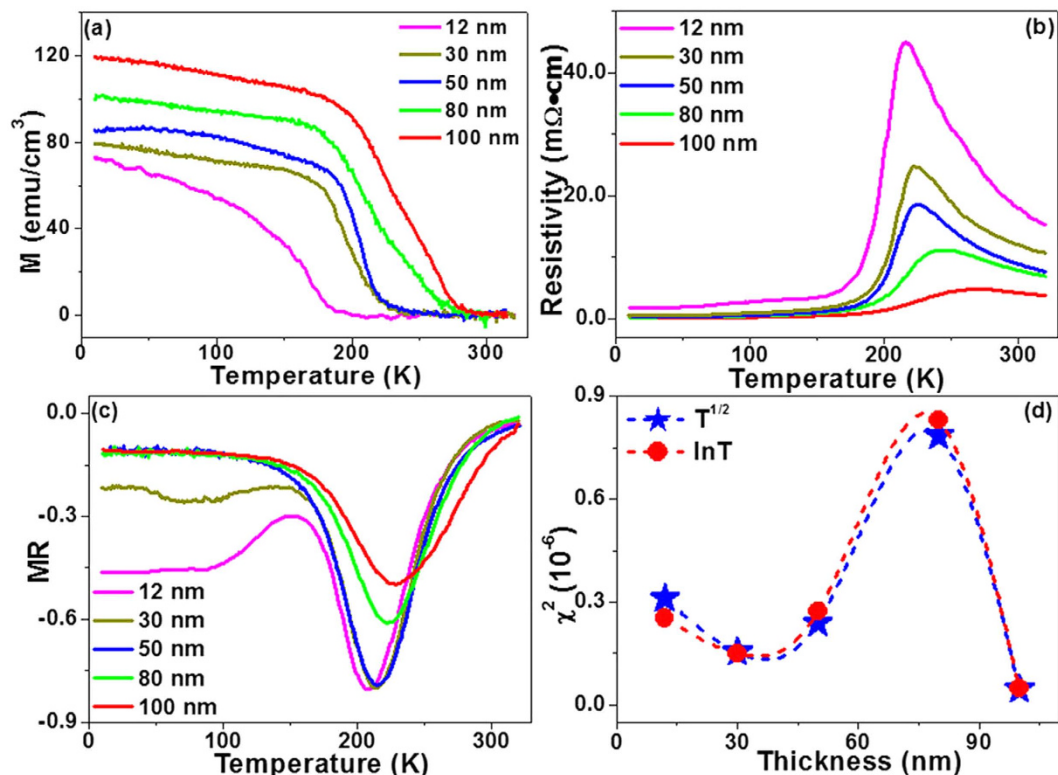


**Figure 6.** (a) the magnetization-temperature (MT) curves of PSMO films with different thicknesses, measured with a field of 100 Oe; (b) resistance-temperature (RT) curves at 0T and (c) Magnetoresistance (MR) of PSMO film with a magnetic field of 4T; (d) The change of  $\chi^2$  with film thickness. The red dot refers to equation (1) and the blue star refers to equation (2). Refer to the text for more information.

shows an increase of MR value with decreasing film thickness at low temperature (10–100 K). Weak electronic localization in thin film may produce large negative MR effects<sup>46</sup> at low temperature. Details of the 3D-to-2D cross over as a function of film thickness warrant further study, which is beyond the current scope of investigation.

The double-exchange model suggests that the exchange interaction intensity is proportional to the averaged electron hopping possibility<sup>47–51</sup> between the two neighboring Mn sites ( $t_{d-d}$ ) and  $T_c$ . In the case of weak strain, strain relaxation affects the crystal structure and  $T_c$  of manganite films may be calculated according to the following equation<sup>48</sup>:

$$T_c(\varepsilon_b, \varepsilon_{JT}) = T_{c0}(1 - a\varepsilon_b - 1/2b\varepsilon_{JT}^2) \quad (3)$$

where  $\varepsilon_b = (2\varepsilon_{100} + \varepsilon_{001})$  is the bulk strain,  $\varepsilon_{JT} = \sqrt{2/3}(\varepsilon_{100} - \varepsilon_{001})$  is the Jahn-Teller strain,  $a = \left(\frac{1}{T_c}\right)\left(\frac{dT_c}{d\varepsilon_b}\right) \sim 10$  and  $b = \left(\frac{1}{T_c}\right)\left(\frac{dT_c}{d\varepsilon_{JT}^2}\right) \sim 500^{25}$ .

Calculated values of  $T_c$  using equation (3) increased with increasing film thickness, consistent with the experimental results as shown in Fig. 6(a) and in Table 1. Note that for calculations involving the 80-nm and 100-nm films, the averaged lattice constant was used (from the area ratio of volume-averaged XRD results, see Supplementary Figure S2 online). The discrepancy between experimental and calculated values may arise from ignoring the effects of inhomogeneous crystal structure through film thickness and orbital reconstruction<sup>29–32</sup>. In the 100-nm film, strain relaxation weakened the anisotropy in the local environment and enhanced the electronic hopping probability. For the 12-nm film with the lowest  $T_c$ , the effects of interface may be important and warrant further investigation.

In summary, the effects of thickness-dependent strain relaxation on  $\text{Pr}_{0.67}\text{Sr}_{0.33}\text{MnO}_3$  film properties were investigated. The films showed in-plane compressive strain and out-of-plane tensile strain. Strain relaxation occurred with increasing film thickness, affecting both the lattice constant and  $\text{MnO}_6$  octahedral rotation. These in turn influenced the corresponding electronic structures. In polarization dependent measurements, the in-plane and out-of-plane XANES were anisotropic with different absorption energy  $E_r$ . With increasing film thickness, the difference of  $E_r$  between the two polarization dependent measurements decreased. Based on the XRD results, the strain relaxation weakened the local anisotropy and probability of charge transfer (between Mn 3d and O 2p orbitals) along the in-plane and out-of-plane directions, giving rise to the change in  $E_r$ . The magnetoresistance effect and Curie temperature of PSMO films also showed variation with strain relaxation.

## Methods

**Film fabrication.**  $\text{Pr}_{0.67}\text{Sr}_{0.33}\text{MnO}_3$  (PSMO) films with different thicknesses (12, 30, 50, 80 and 100 nm) were grown on (001)  $\text{LaAlO}_3$  (LAO) single crystal substrates using a 248 nm KrF pulsed laser at a substrate temperature of 780 °C and a pure oxygen pressure of 26 Pa. The energy of the laser beam was 90 mJ and the pulse frequency was 5 Hz. After deposition, the films were cooled to room temperature at 20 K/min.

**Characterization.** X-ray diffraction (XRD) was measured using four-circle diffractometer at the Singapore Synchrotron Light Source (SSLS) with  $\text{CuK}_{\alpha 1}$  radiation equivalent. The magnetic properties were measured by a superconducting quantum interference device (SQUID), and the transport properties were measured by Physical Property Measurement System (PPMS). The polarization dependent XANES measurements were performed using linear polarized X-rays at beamline 20-ID-B of the Advanced Photon Source (APS), Argonne National Laboratory, USA. Fluorescent X-rays were detected using a multi-element germanium detector, and the XANES normalization was done using Athena. Details on the beamline optics and instruments may be found elsewhere<sup>25,26</sup>. A Mn metal foil was placed to intercept a scattered beam for monochromator energy calibration.

## References

- Dagotto, E., Hotta, T. & Moreo, A. Colossal magnetoresistant materials: the key role of phase separation. *Phys. Rep.* **344**, 1–153 (2001).
- Haghir-Gosnet, A.-M. & Renard, J.-P. CMR manganites: physics, thin films and devices. *J. Phys. D: Appl. Phys.* **36** R127–R150 (2003).
- Gambardella, A. *et al.* Surface Nanostructures in Manganite Films. *Sci. Rep.* **4**, 5353; doi: 10.1038/srep05353 (2014).
- Yin, Y. W. *et al.* Enhanced tunnelling electroresistance effect due to a ferroelectrically induced phase transition at a magnetic complex oxide interface. *Nature Mater.* **12**, 397–402 (2013).
- Zhou, S. Y. *et al.* Glass-like recovery of antiferromagnetic spin ordering in a photo-excited manganite  $\text{Pr}_{0.7}\text{Ca}_{0.3}\text{MnO}_3$ . *Sci. Rep.* **4**, 4050; doi: 10.1038/srep04050 (2014).
- Peng, H. Y. *et al.* Effects of electrode material and configuration on the characteristics of planar resistive switching devices. *APL Materials* **1**, 052106; doi: 10.1063/1.4827597 (2013).
- Guo, D. Y. *et al.* Unipolar resistive switching behavior of amorphous gallium oxide thin films for nonvolatile memory applications. *Appl. Phys. Lett.* **106**, 042105 (2015).
- Cheng, X., Sullaphen, J., Weyland, M., Liu, H. & Valanoor, N. Role of interface structure and chemistry in resistive switching of NiO nanocrystals on  $\text{SrTiO}_3$ . *APL Materials* **2**, 032109; doi: 10.1063/1.4869457 (2014).
- Imada, M., Fujimori, A. & Tokura, Y. Metal-insulator transitions. *Rev. Mod. Phys.* **70**, 1039–1263 (1998).
- Pesquera, D. *et al.* Surface symmetry-breaking and strain effects on orbital occupancy in transition metal perovskite epitaxial films. *Nat. Commun.* **3**, 1189 (2012).
- Ankudinov, A. L., Ravel, B., Rehr, J. J. & Conradson, S. D. Real-space multiple-scattering calculation and interpretation of x-ray-absorption near-edge structure. *Phys. Rev. B* **58**, 7565–7576 (1998).
- Abad, L. *et al.* Interfacial Strain: The Driving Force for Selective Orbital Occupancy in Manganite Thin Films. *Adv. Funct. Mater.* **17**, 3918–3925 (2007).
- Kyoungsook Jin, K. *et al.* Partially Oxidized Sub-10 nm MnO Nanocrystals with High Activity for Water Oxidation Catalysis. *Sci. Rep.* **5**, 10279; doi: 10.1038/srep10279 (2015).
- Qiao, R., Chin, T., Harris, S. J., Yan, S. & Yang, W. Spectroscopic fingerprints of valence and spin states in manganese oxides and fluorides. *Curr. Appl. Phys.* **13**, 544e548 (2013).
- Brown, E. G. Jr. & Waychunas, A. G. X-ray Absorption Spectroscopy: Introduction to Experimental Procedures. Available at: [http://www-ssrl.slac.stanford.edu/mes/xafs/xas\\_intro.html](http://www-ssrl.slac.stanford.edu/mes/xafs/xas_intro.html). (Accessed: 19th November 2004).
- Sun, C. J. *et al.* Directional short range order in  $L1_0$  FeMnPt magnetic thin films. *Phys. Rev. B* **84**, 140408(R) (2011).
- Magnuson, M. *et al.* Self-doping processes between planes and chains in the metal-to-superconductor transition of  $\text{YBa}_2\text{Cu}_3\text{O}_{6.9}$ . *Sci. Rep.* **4**, 7017; doi: 10.1038/srep07017 (2014).
- Chen, J. M. *et al.* Pressure-dependent electronic structures and orbital hybridization of Mn 3d states in multiferroic  $\text{BiMnO}_3$ : A combined x-ray absorption, x-ray emission, and resonant x-ray emission study. *Phys. Rev. B* **86**, 045103 (2012).
- Horiba, K. *et al.* Nature of the Well Screened State in Hard X-Ray Mn 2p Core-Level Photoemission Measurements of  $\text{La}_{1-x}\text{Sr}_x\text{MnO}_3$  Films. *Phys. Rev. Lett.* **93**, 236401 (2004).
- Tolentino, H. *et al.* Anisotropy of the core-hole relaxation in x-ray-absorption spectroscopy as probed in square planar cuprates. *Phys. Rev. B* **45**, 8091–8096 (1992).
- Zhang, B. *et al.* Strain modulated anisotropic electronic charge transfer in perovskite  $\text{Pr}_{0.67}\text{Sr}_{0.33}\text{MnO}_3$  thin films. *Phys. Rev. B* **89**, 195140 (2014).
- M. Calandra, M. *et al.* K-edge x-ray absorption spectra in transition-metal oxides beyond the single-particle approximation: Shake-up many-body effects. *Phys. Rev. B* **86**, 165102 (2012).
- Moon, E. J., Keavney, D. J. & May, S. J. Strain Effects in Narrow-Bandwidth Manganites: The Case of Epitaxial  $\text{Eu}_{0.7}\text{Sr}_{0.3}\text{MnO}_3$  Thin Films. *Phys. Rev. Applied* **1**, 054006 (2014).
- Martin, C., Maignan, A., Hervieu, M. & Raveau, B. Magnetic phase diagrams of  $L_{1-x}A_x\text{MnO}_3$  manganites. *Phys. Rev. B* **60**, 12191–12199 (1999).
- Wang, H. S., Wertz, S. E., Hu, Y. F., Li, Q. & Schlom, D. G. Role of strain in magnetotransport properties of  $\text{Pr}_{0.67}\text{Sr}_{0.33}\text{MnO}_3$  thin films. *J. Appl. Phys.* **87**, 7409–7414 (2000).
- Yang, P., Liu, H., Chen, Z., Chen, L. & Wang, J. Unit-cell determination of epitaxial thin films based on reciprocal-space vectors by high-resolution X-ray Diffractometry. *J. Appl. Cryst.* **47**, 402–413 (2014).
- MacLaren, I., Wang, Z. L., Wang, H. S. & Li, Q. Strain-induced crystal structure change in ultrathin films of  $\text{Pr}_{0.7}\text{Sr}_{0.3}\text{MnO}_3$ . *Appl. Phys. Lett.* **80**, 1406–1408 (2002).
- Sheng, Z. G., Gao, J. & Sun, Y. P. Coaction of electric field induced strain and polarization effects in  $\text{La}_{0.7}\text{Ca}_{0.3}\text{MnO}_3/\text{PMN-PT}$  structures. *Phys. Rev. B* **79**, 174437 (2009).
- Konishi, Y. *et al.* Orbital-State-Mediated Phase-Control of Manganites. *J. Phys. Soc. Jpn.* **68**, 3790–3793 (1999).
- Fang, Z., Solovyev, I. V. & Terakura, K. Phase Diagram of Tetragonal Manganites. *Phys. Rev. Lett.* **84**, 3169–3172 (2000).
- Fang, Z. & TERAKURA, K. Surface Magnetic Phase Diagram of Tetragonal Manganites. *J. Phys. Soc. Jpn.* **70**, 3356–3361 (2001).
- Park, J.-H., Kimura, T. & Tokura, Y. Competition between lattice distortion and charge dynamics for the charge carriers of double-layered manganites. *Phys. Rev. B* **58**, R13330–R13333 (1998).
- Glazer, A. M. The Classification of Tilted Octahedra in Perovskites. *Acta Crystallogr., Sect. B: Struct. Crystallogr. Cryst. Chem.* **28**, 3384 (1972).
- Glazer, A. M. Simple Ways of Determining Perovskite Structures. *Acta Crystallogr., Sect. A: Crystal Physics, Diffraction, Theoretical and General Crystallography* **31**, 756 (1975).

35. Woodward, P. M. Octahedral Tilting in Perovskites. I. Geometrical Considerations. *Acta Crystallogr., Sect. B: Struct. Sci.* **53**, 32 (1997).
36. Woodward, P. M. Octahedral Tilting in Perovskites. II. Structure Stabilizing Forces. *Acta Crystallogr., Sect. B: Struct. Sci.* **53**, 44 (1997).
37. Qian, Q. *et al.* Local structural distortions in manganites probed by comparative x-ray-emission and x-ray-absorption near-edge measurements. *Phys. Rev. B*, **64**, 024430 (2001).
38. Liu, M. F. *et al.* Unusual ferromagnetism enhancement in ferromagnetically optimal manganite  $\text{La}_{0.7-y}\text{Ca}_{0.3+y}\text{Mn}_{1-y}\text{Ru}_y\text{O}_3$  ( $0 \leq y < 0.3$ ): the role of Mn-Ru  $t^{2g}$  super-exchange. *Sci. Rep.* **4**, 9922; doi: 10.1038/srep09922 (2015).
39. Cooper, S. L. *et al.* Optical studies of gap, exchange, and hopping energies in the insulating cuprates. *Phys. Rev. B* **42**, 10785–10788 (1990).
40. Moskvin, A. S. One-center charge transfer transitions in manganites. *Phys. Rev. B*, **65**, 205113 (2002).
41. Baublitz, M. *et al.* A Minimal tight-binding model for ferromagnetic canted bilayer manganites. *Sci. Rep.* **4**, 7512; doi: 10.1038/srep07512 (2014).
42. Heald, S. M., Cross, J. O., Brewes, D. L. & Gordon, R. A. The PNC/XOR X-ray microprobe station at APS sector 20. *Nucl. Instrum. Methods Phys. Res. A* **582**, 215–217 (2007).
43. Sterbinsky, G. E. *et al.* Local atomic and electronic structures of epitaxial strained  $\text{LaCoO}_3$  thin films. *Phys. Rev. B* **85**, 020403 (2012).
44. Maritato, L. *et al.* Low-temperature resistivity of  $\text{La}_{0.7}\text{Sr}_{0.3}\text{MnO}_3$  ultra thin films: Role of quantum interference effects. *Phys. Rev. B* **73**, 094456 (2006).
45. Kumar, D., Sankar, J., Narayan, J., Singh, R. K. & Majumdar, A. K. Low-temperature resistivity minima in colossal magnetoresistive  $\text{La}_{0.7}\text{Ca}_{0.3}\text{MnO}_3$  thin films. *Phys. Rev. B* **65**, 094407 (2002).
46. Wang, C. Magnetoelectric transport and quantum interference effect in ultrathin manganite films. *Appl. Phys. Lett.* **104**, 162405 (2014).
47. Anderson, P. W. & Hasegawa, H. Considerations on Double Exchange. *Phys. Rev.* **100**, 675–681 (1955).
48. Millis, A. J., Darling, T. & Migliori, A. Quantifying strain dependence in “colossal” magnetoresistance manganites. *J. Appl. Phys.* **83**, 1588–1591 (1998).
49. Millis, A. J. Cooperative Jahn-Teller effect and electron-phonon coupling in  $\text{La}_{1-x}\text{A}_x\text{MnO}_3$ . *Phys. Rev. B* **53**, 8434–8441 (1996).
50. Millis, A. J., Littlewood, P. B. & Shraiman, B. I. Double exchange alone does not explain the resistivity of  $\text{La}_{1-x}\text{Sr}_x\text{MnO}_3$ . *Phys. Rev. Lett.* **74**, 5144–5147 (1995).
51. Millis, A. J., Shraiman, B. I. & Mueller, R. Dynamic Jahn-Teller Effect and Colossal Magnetoresistance in  $\text{La}_{1-x}\text{Sr}_x\text{MnO}_3$ . *Phys. Rev. Lett.* **77**, 175–178 (1996).

## Acknowledgements

Work at the National University of Singapore is supported by the Singapore National Research Foundation under CRP Award No. NRF-CRP10-2012-02. PNC/XSD facilities at the Advanced Photon Source, and research at these facilities, are supported by the US Department of Energy - Basic Energy Sciences, the Canadian Light Source and its funding partners, the University of Washington, and the Advanced Photon Source. Use of the Advanced Photon Source, an Office of Science User Facility operated for the U.S. Department of Energy (DOE) Office of Science by Argonne National Laboratory, was supported by the U.S. DOE under Contract No. DE-AC02-06CH11357. PY is supported by SSSL via NUS Core Support C-380-003-003-001.

## Author Contributions

B.M.Z., C.J.S. and P.Y. conducted the experiments; B.M.Z., C.J.S., G.M.C. analyzed the data; B.M.Z., J.S.C., C.J.S. and G.M.C. wrote the manuscript; B.M.Z., J.S.C., P.Y., X.C., W.N.L., T.V., C.J.S., S.M.H. and G.M.C. reviewed the manuscript.

## Additional Information

**Supplementary information** accompanies this paper at <http://www.nature.com/srep>

**Competing financial interests:** The authors declare no competing financial interests.

**How to cite this article:** Zhang, B. *et al.* Effects of strain relaxation in  $\text{Pr}_{0.67}\text{Sr}_{0.33}\text{MnO}_3$  films probed by polarization dependent X-ray absorption near edge structure. *Sci. Rep.* **6**, 19886; doi: 10.1038/srep19886 (2016).



This work is licensed under a Creative Commons Attribution 4.0 International License. The images or other third party material in this article are included in the article’s Creative Commons license, unless indicated otherwise in the credit line; if the material is not included under the Creative Commons license, users will need to obtain permission from the license holder to reproduce the material. To view a copy of this license, visit <http://creativecommons.org/licenses/by/4.0/>